
# CO-Induced Structural Flexibility in Cu and Au Nano-Catalysts

*ChemCatChem*

ChemCatChem
Chemistry Europe
European Chemical Societies Publishing

RESEARCH ARTICLE OPEN ACCESS

# CO-Induced Structural Flexibility in Cu and Au Nano-Catalysts

Rasmus Svensson | Alvaro Posada-Borbón | Henrik Grönbeck

Department of Physics and Competence Centre for Catalysis, Chalmers University of Technology, Göteborg, Sweden

**Correspondence:** Rasmus Svensson (rassve@chalmers.se) | Alvaro Posada-Borbón (palvaro@chalmers.se) | Henrik Grönbeck (ghj@chalmers.se)

**Received:** 29 August 2025 | **Revised:** 9 December 2025 | **Accepted:** 23 December 2025

## ABSTRACT

Catalyst nanoparticles are dynamic, and their structures depend on the reaction conditions. Although average shapes can be observed experimentally, it is challenging to monitor transient structures and the mechanisms for structural changes during operating conditions. Herein, we use Density Functional Theory-based kinetic Monte Carlo simulations to study how CO affects adatom formation and clustering on Cu and Au surfaces and nanoparticles. Adatoms are created at undercoordinated sites and are stabilized by the formation of metal–CO complexes. Clusters of adatoms are formed on the (100) facets for both metals. The clusters are transient for Au, whereas they can be regarded as precursors for Cu nanoparticle reshaping. Bulk vacancies are present for Au, whereas vacancies are mainly located in the surface layer for Cu. The work demonstrates the structural flexibility of Au and Cu nanoparticles in the presence of an adsorbate, which has consequences for their catalytic properties.

## 1 | Introduction

Material properties generally depend on the atomic structure, and large efforts are directed to establishing structure–function relationships. In heterogeneous catalysis, such efforts include studies where catalytic properties are investigated for well-characterized surface facets and nanoparticles (NPs) with controlled shapes and sizes. One challenge when investigating structure–function relationships in heterogeneous catalysis is the inherent flexibility of metal NPs in the typical size range of 2–5 nm. Adsorption may alter the relative stability of different facets, which may lead to refacetting and reshaping [1, 2], or eventually the formation of different phases, such as oxides and carbides [3]. An illustrative example of the dynamic character of catalyst surfaces is the self-sustained chemical oscillations during $H_2$ oxidation over Ru surfaces [4], where the periodic, facet-dependent formation of oxidized Ru determines the activity of the catalyst.

The time-scales for reshaping and the formation of different phases are in some cases slow enough to be followed experimentally using, for example, spectroscopy [5] or transmission electron microscopy [6]. However, many structural changes are fast and transient and therefore difficult to capture with conventional experimental techniques at operating conditions. One example is the transient formation of adatoms, which could be promoted by adsorbates such as CO. CO oxidation on Au NPs supported on ceria has been proposed to occur on transient adatom species [7]. Based on ab initio molecular dynamics, it was in Ref. [7] suggested that gold cations detach from the Au NPs and catalyze CO oxidation on the oxide as single atom catalysts. Although molecular dynamics simulations provide detailed information on reaction mechanisms, such simulations are limited to time-scales of ps–ns, which is too short to capture extensive restructuring. Because of the separation of time-scales, it is computationally challenging to simultaneously treat chemical transformations and the structural flexibility of metal NPs. The structural dynamics and/or thermodynamical stability of metal NPs have in the past been investigated using molecular dynamics [8, 9] or (kinetic) Monte Carlo simulations [10–14], whereas simulations of reaction kinetics have been performed on static catalysts using mean-field or kinetic Monte Carlo approaches [15–17].

Recent efforts have been taken to combine the structural flexibility of NPs and reaction kinetics [18–20]. Based on Density Functional Theory (DFT) informed kinetic Monte Carlo simulations, it was recently proposed that small metal clusters may form on stepped metal surfaces in the presence of adsorbates such as CO and $NH_3$ [18]. Similarly, DFT-based kinetic Monte Carlo simulations for dilute Pd@Au NPs in the presence of CO have revealed that CO promotes the presence of Pd atoms in the surface of Au NPs and the formation of small transient Au clusters [19]. Hydrogen and CO facilitated surface roughening of Cu has, moreover, been proposed using pseudo kinetic Monte Carlo simulations during conditions for electroreduction of $CO_2$ [12]. The formation of undercoordinated sites is particularly important for the catalytic properties of metal NPs, which are described by linear scaling relations. Brønsted–Evans–Polanyi relations link reaction barriers with adsorption energies, which are determined by the local metal coordination numbers. Using such scaling relations, CO-induced roughening of Pt NPs has recently been shown to produce fluctuating catalytic activity for the CO oxidation reaction [20].

Herein, we apply DFT-based kinetic Monte Carlo simulations to compare adatom formation in the presence of CO on Cu and Au surfaces and NPs. The potential energy surfaces are constructed from DFT calculations for different surface structures using scaling relations based on coordination numbers. CO is found to promote adatom formation and the presence of small two-dimensional clusters. The clusters formed on Au are transient, whereas the clusters on Cu can be regarded as the initial phase of NP reshaping.

## 2 | Computational Approaches

The kinetic behavior of Au and Cu surfaces and NPs is investigated using kinetic Monte Carlo simulations, based on scaling relations. The scaling relations are derived from energies obtained from DFT calculations.

### 2.1 | Density Functional Theory Calculations

Density functional theory calculations are performed with the Vienna Ab Initio Simulation Package (VASP) [21–24]. The interaction between the core and valence electrons is described with the projector-augmented wave (PAW) method [25, 26]. The considered valence electrons are $2s^2 2p^2$ (C), $2s^2 2p^4$ (O), $3d^{10} 4s^1$ (Cu), and $5d^{10} 6s^1$ (Au). The exchange-correlation effects are described with the functional proposed by Perdew, Burke, and Ernzerhof (PBE) [27]. Dispersive interactions are accounted for using the D3-correction [28, 29]. The Kohn–Sham orbitals are expanded with plane waves, truncated at 450 eV. The electronic structure is considered to be converged when the changes in Kohn–Sham eigenvalues and electronic energies are below 1e-6 eV.

The potential energy landscape is constructed from explicit calculations of the extended (111), (100), (211), and (532) surfaces. The (111) and (100) surfaces are described by $p(3\times3)$ surface cells, the (211) surfaces by $p(1\times3)$ surface cells, and the (532) surfaces by $p(1\times1)$ surface cells. The surface slabs consist of six atomic layers, of which the two bottom layers are kept fixed in their bulk positions. The periodic slabs are separated by at least 14 Å of vacuum. The integration of the Brillouin zone is approximated by finite sampling using a Γ-centered (7,7,1) and (5,5,1) grid for Au and Cu, respectively. Bulk calculations are done with a $(3 \times 3 \times 2)$ unit cell (72 atoms) using a (3,3,5) k-point grid. Structural optimization is performed using the conjugate gradient method, and structures are considered to be converged when the maximum force on each nuclei is below 0.03 eV/Å. Transition state structures are obtained using the climbing image nudged elastic band (CI-NEB) method [30, 31]. The reference energy of gas phase CO is calculated using a (30, 31, 32) Å vacuum box, sampled by the Γ-point. Vibrational analyses are performed using finite differences within the harmonic approximation.

### 2.2 | Kinetic Monte Carlo Simulations

The reaction kinetics of CO adsorption, desorption, and metal diffusion are investigated using kinetic Monte Carlo (kMC) simulations. kMC is a stochastic approach, where the structures are evolved over time [32, 33]. In the first reaction method, a list of possible events ($L$) is created, which connects specific states of the system. Each possible event is associated with a time of occurrence ($t_{\text{occ.}}$) according to

$$t_{\text{occ}} = t_{\text{sim}} - \frac{\ln u}{k}, \tag{1}$$

where $t_{\text{sim}}$ is the current time of the simulation, $u$ is a uniform random number in the unit interval, and $k$ is the rate constant for the specific event, which in this case is an elementary reaction. In each step of the kMC simulation, the event with the lowest $t_{\text{occ}}$ is executed. The system is updated according to the chosen event, and $t_{\text{sim}}$ is set to $t_{\text{occ}}$. After the update, events that are disabled are removed from $L$, and new events that have been enabled are added to $L$. New times of occurrences are evaluated for events where the reaction rate constant has changed because of the structural update.

The rate constant for CO adsorption is described using collision theory [34]

$$k_{\text{ads}} = \frac{pAs_0}{\sqrt{2\pi m k_{\text{B}} T}}, \tag{2}$$

where $p$ is the pressure, $A$ is the area of the adsorption site, $s_0$ is the sticking coefficient (assumed to be 1), $m$ is the mass of CO, $k_{\text{B}}$ is the Boltzmann constant, and $T$ is the temperature. Thermodynamic consistency is ensured by computing the rate constant for desorption from the adsorption rate constant via the equilibrium constant

$$K = \frac{k_{\text{ads}}}{k_{\text{des}}} = \mathrm{e}^{-\Delta G/k_{\text{B}}T} \iff k_{\text{des}} = k_{\text{ads}} \mathrm{e}^{\Delta G/k_{\text{B}}T}, \tag{3}$$

where $\Delta G$ is the zero-point corrected free energy of adsorption. The partition function of adsorbed CO is calculated assuming frustrated vibrations as follows:

$$Z_{\text{vibration}} = \prod_i \frac{1}{1 - \mathrm{e}^{-\varepsilon_i/k_{\text{B}}T}}, \tag{4}$$

where $\varepsilon_i$ is the energy of vibrational mode $i$. The gas phase partition function is calculated as the product between the translational, rotational, and vibrational partition functions

$$Z = Z_{\text{translation}} Z_{\text{rotation}} Z_{\text{vibration}} = \frac{k_B T}{p} \left( \frac{\sqrt{2\pi m k_B T}}{h} \right)^3 \frac{8\pi^2 I k_B T}{h^2} \frac{1}{1 - e^{-\varepsilon / k_B T}}, \quad (5)$$

where $m$ is the mass of CO, $h$ is Planck's constant, $I$ is the moment of inertia, and $\varepsilon$ is the C—O stretch vibrational energy. The elementary reaction rate constants are calculated from transition state theory according to

$$k \approx \frac{k_B T}{h} e^{-E^{\ddagger} / k_B T}, \quad (6)$$

where $E^{\ddagger}$ is the energy difference between the transition and initial states.

A common issue in kMC simulations is that different types of events often are associated with different time-scales [32]. One method to prevent sampling of only the fastest event is to scale some rate constants. Here, we have scaled CO adsorption/desorption to/from the metal site, see Supporting Information. Because of the fast CO adsorption/desorption, CO diffusion is not explicitly included in the simulation as adsorption/desorption equilibrates the CO coverage on the time scale of vacancy formations. Comparative simulations including CO diffusion as a reaction event are presented in the Supporting Information (Figure S1).

### 2.2.1 | Considered Elementary Reactions

The considered events include CO adsorption/desorption and events for metal diffusion. The events with metal atoms include processes where vacancies are formed/healed, diffusion between the surface and the bulk, and adatom diffusion events. As elementary reactions could be concerted mechanisms including more than one metal atom, processes where two metal atoms move simultaneously are also incorporated. The considered elementary reactions are as follows:

$$\text{CO(g)} + * \;\text{<=>}\; \text{CO}^* \quad \text{(R1)}$$

$$\text{M} + * \;\text{<=>}\; \circ + \text{M}^* \quad \text{(R2)}$$

$$\text{M–CO} + * \;\text{<=>}\; \circ + (\text{M–CO})^* \quad \text{(R3)}$$

$$\text{CO(g)} + \text{M}^* \;\text{<=>}\; (\text{M–CO})^* \quad \text{(R4)}$$

$$(\text{M–2CO})^* + \circ \;\text{->}\; \text{CO}^* + \text{M–CO} \quad \text{(R5)}$$

$$\text{M}^* + * \;\text{<=>}\; * + \text{M}^* \quad \text{(R6)}$$

$$(\text{M–CO})^* + * \;\text{<=>}\; * + (\text{M–CO})^* \quad \text{(R7)}$$

$$(\text{M–2CO})^* + * \;\text{<=>}\; * + (\text{M–2CO})^* \quad \text{(R8)}$$

$$\text{M} + \circ \;\text{<=>}\; \circ + \text{M} \quad \text{(R9)}$$

$$\text{M–CO}^* + \circ \;\text{<=>}\; \circ + \text{M–CO}^* \quad \text{(R10)}$$

where M is either Au or Cu, $*$ denotes an empty surface site, and $\circ$ denotes a vacancy. $M^*$ denotes an adatom and M denotes a metal atom in the metal NP. Reaction (R1) describes the adsorption and desorption of CO. Reaction (R2) describes the formation and healing of a surface vacancy. In (R2), an atom in the surface layer forms an adatom on a neighboring surface site. The formation and healing processes can occur either with one metal atom or via a concerted mechanism with two metal atoms. The process with the lowest barrier is implemented in the kMC simulations. For Au, the concerted mechanism is significantly favored for (111), (100), and for steps where the coordination of the adatom decreases with 7, 6, and 4, respectively, as compared to the atom in the surface. However, for cases where the adatom coordination is reduced by 3 with respect to the surface atom (for example, a (211) step toward a micro(100) facet, and the corner of a (532) surface toward the (111) facet), the one-atom mechanism is favored. For Cu, the formation of a vacancy occurs via the one-atom mechanism in cases where the coordination of the surface atom $\leq 7$. On the (111) surface and on the (100) surface, the concerted mechanism is favored. However, the preference for the concerted mechanism is not as pronounced as for Au. Reaction (R3) describes the CO-mediated formation and healing of a vacancy. In the CO-mediated process, CO adsorbed on a metal atom in the surface layer is ejected to form a metal–CO adatom complex on a neighboring surface site. Reaction (R4) describes the adsorption and desorption of CO from an adatom on the surface. A second CO molecule can be adsorbed on the (M—CO)* complex, albeit, the adsorption energy of a second CO molecule is weak. Reaction (R5) denotes the healing of a vacancy, in which the process is mediated by two CO molecules. After the healing, one CO molecule is adsorbed on the metal atom, whereas the other CO molecule resides on a neighboring site on the surface. Reaction (R6) describes adatom diffusion on the metal surface. This process occurs either via the diffusion of one metal atom, or a simultaneous movement of an adatom and a surface atom. The process with the lowest barrier is implemented in the kMC simulations. For Au, the simultaneous movement of two atoms is associated with the lowest diffusion barrier on the (100) surface and over a (211) step, whereas adatom diffusion (one atom) is favored on the (111) surface. On Cu, the simultaneous movement of two metal atoms for the diffusion is only favored when the

diffusion occurs over a (211) step. Reactions (R7) and (R8) are the diffusion of M—CO and M—2CO complexes, respectively. Reaction (R9) describes the diffusion of a metal atom (not an adatom) to a neighboring vacancy, either in the surface, between surface layers, or in the bulk. Reaction (R10) is the CO-mediated diffusion of a surface atom to a neighboring surface vacancy. A complete description on how the initial, final and transition state energies are obtained for the different events is presented in the Supporting Information.

## 3 | Results and Discussion

### 3.1 | Potential Energy Surfaces

DFT calculations for a range of different systems (see Supporting Information) are performed to establish scaling relations for the stability of the metal atom. The scaling relations for the energy (in eV) of a metal atom as a function of the coordination number (CN) are,

$$E(\mathrm{Au}) = -2.226 - 0.245 \times \mathrm{CN} \tag{7}$$

$$E(\mathrm{Cu}) = -2.160 - 0.304 \times \mathrm{CN}. \tag{8}$$

The energy for CO adsorption is calculated for coordination numbers 2–10 and the explicit values are used in the kMC simulations. The diffusion barrier for CO-decorated metal atoms $E^{\ddagger}$ (M—CO) is described by

$$E^{\ddagger}(M-CO) = E^{\ddagger}(\mathrm{M}) + E^{\mathrm{TS}}_{\mathrm{ads}}(\mathrm{CO}) - E^{\mathrm{IS}}_{\mathrm{ads}}(\mathrm{CO}) \tag{9}$$

$E^{\ddagger}(\mathrm{M})$ is the barrier in the absence of CO. $E^{\mathrm{TS}}_{\mathrm{ads}}(\mathrm{CO})$ and $E^{\mathrm{IS}}_{\mathrm{ads}}(\mathrm{CO})$ are the adsorption energies of CO on the metal atom in the transition state (TS) and initial state (IS), respectively. The CO adsorption energy as a function of coordination number is presented in Figure 1. For CO adsorbed in bridge or hollow configurations, the CN corresponding to the atop configuration of the specific adsorption site is chosen in the kMC simulations. The CO adsorption strength decreases linearly with the CN and the slope is greater for Au than for Cu. CO—CO repulsive interactions are considered for CO on neighboring metal sites. The interaction is considered to be two-body and determined by calculations for Au(111) to be 0.14 eV.

The potential energy surfaces (PESes) for the formation of an adatom/vacancy pair and the subsequent formation of a cluster on the surface are shown in Figure 2. The left panels show the process in the absence of CO, whereas the right panels show the CO-mediated processes. The PESes are constructed for different origins of the adatom, namely (111), (100), (211), and (532). (211) and (532) represent edges and corners, and the adatoms are in these cases assumed to be ejected onto a (111) facet. Structural models for the process of adatom creation and cluster formation is shown for (111). The ejected adatom is on the (111) facet coalescing with a preexisting dimer, forming a trimer, whereas the adatom on (100) is coalescing with a preexisting trimer, forming a tetramer. By choosing different sizes of the preexisting clusters, the change

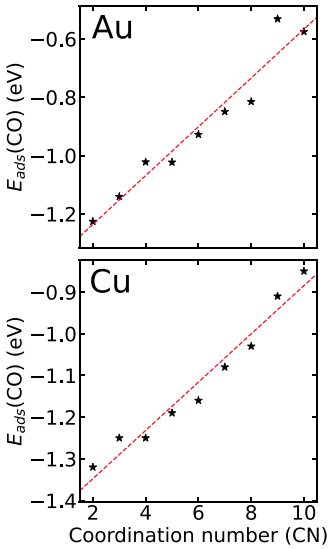


**FIGURE 1** | The CO adsorption energy for different coordination numbers in the range 2–10, for Au (top) and Cu (bottom). The red, dashed lines are guides for the eye.

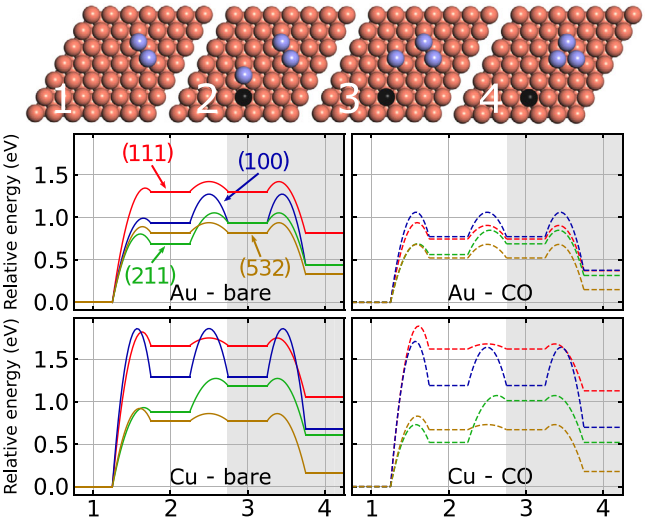


**FIGURE 2** | The potential energy landscapes for the cluster formation process on the (111) surface [red], (100) surface [blue], (211) surface [green] and (532) surface [brown], for Au (top) and Cu (bottom). In the left figures, the landscapes in the absence of CO are presented, whereas the right figures show the CO-mediated process. The shaded area describes process occurring on the (111) or (100) facets, respectively.

in coordination number for the adatom as the final cluster forms is two on both (111) and (100).

On bare Au(111), the formation of an adatom/vacancy occurs via the concerted mechanism with two Au atoms, and is associated with a barrier of 1.35 eV. The formation of an adatom/vacancy pair is endothermic, and the backward process (vacancy healing) has a low barrier of 0.04 eV. The adatom may diffuse on the surface with a barrier of 0.12 eV. The diffusion barrier of the adatoms on the extended surfaces depends on the number of neighboring adatoms in the initial state. The diffusion barrier toward a cluster is similar to the barrier for a single adatom

diffusing on an extended surface, whereas the diffusion barrier away from a cluster depends on the number of neighboring atoms in the cluster. The formation of a trimer on Au(111) is endothermic by 0.81 eV with respect to the bare surface.

The adatom formation barrier is 0.99 eV on the bare Au(100). The adatom formation occurs also for this surface via the concerted mechanism. The healing of the vacancy, which also includes two atoms, has a low barrier of 0.06 eV. The diffusion of adatom is on the (100) surface less facile than on the (111) surface having a barrier of 0.34 eV. The adatom diffusion on (100) is a two-atom process, where the adatom replaces a surface atom. The healing of the vacancy is strongly favored over the diffusion of the adatom. The formation of a four-atom cluster on Au(100) is endothermic by 0.44 eV with respect to the bare surface. The barrier for adatom/vacancy formation from (211) is reduced to 0.81 eV. The adatom is in this case a one-atom event, and the transition state and the final state of the adatom (in the elementary reaction) are higher coordinated than on both Au(100) and Au(111). The healing of the vacancy has a barrier of 0.12 eV, whereas the diffusion barrier away from the step to the (111) terrace is 0.36 eV. Hence, the adatoms are expected to be short-lived, and the effective barrier to remove the adatom from the step to the (111) facet is $\sim$ 1.05 eV. The endothermicity of the cluster formation is similar to that on Au(100), which can be understood from the relative stabilities of the metal atom in the initial and final positions. The number of nearest neighbor atoms is in both cases decreased by two. On the bare (532) surface, the vacancy formation process occurs via the one-atom mechanism and is associated with a barrier of 0.89 eV. The adatom is after the process located on a (111) site. The barrier for the adatom to diffuse away from the vacancy (0.12 eV) is in this case similar to the barrier for the healing of the vacancy (0.07 eV). Thus, the adatom is expected to be longer lived in this case as compared to the other surfaces. The formation of a trimer is endothermic by 0.33 eV with respect to the bare surface. To summarize, the formation of a cluster is endothermic on all surfaces. However, the barriers for cluster formation and the stabilities of the clusters are sensitive to the choice of surface, and the size of the formed adatom cluster.

The barriers for vacancy formation are decreased in the presence of CO, which can be understood from Equation (9) and Figure 1. The decreased barriers originate from the solvation of the transition state. As the Au atom in the transition state has a lower coordination than the bare surface atom, the adsorption energy of CO is increased, which stabilizes the transition state with respect to the initial configuration. The influence of CO on the one-atom vacancy formation barrier is most pronounced on the surfaces with highly coordinated atoms [(111) and (100)], where the differences in coordination between the initial and transition state configurations are the largest. Importantly, the stability of the formed adatom–CO complex is considerably stabilized as compared to the adatom in the absence of CO. Consequently, the barrier of the adatom–CO complex diffusion away from the vacancy is similar to the barrier for the vacancy healing process, which extends the lifetime of the vacancy. The stabilities of the final clusters are, in all cases, stabilized in the presence of CO.

For the bare Cu systems, the highest barriers for adatom creation are calculated for Cu(111) and Cu(100), in similarity with Au. A difference with respect to Au is, however, the high barrier on Cu(100). Adatoms are for both surfaces formed preferably via the concerted mechanism. The difference between the barriers computed for the concerted and the one-atom mechanism is, however, small for Cu(100). The barrier is reduced from 1.93 eV (single-atom mechanism) to 1.86 eV (concerted mechanism). The reduction of the barrier is more pronounced on Au(100) where it is 1.46 eV for the one-atom mechanism and 0.99 eV for the concerted mechanism. The difference in importance of the the two mechanisms is related to the softer phonon spectrum for Au. As for Au, the barriers are significantly lower for Cu(211) and Cu(532) surfaces. The reduction of the barriers is again related to the smaller differences in coordination number of the adatom in the initial and transition states.

Adatom formation is endothermic on all Cu-surfaces. The energy differences between (111) and (100) with respect to (211) and (532) is a result of the under-coordination of Cu atoms in (211) and (532). The formation of adatoms is followed by adatom diffusion and cluster formation. The barrier to diffuse away from the vacancy is low on Cu(111), whereas it is larger on Cu(100) and Cu(211) because of the comparably high loss of coordination of the adatom at the transition state in this case. The addition of the adatom to the pre-existing cluster is exothermic by around 0.6 eV in all cases.

The adsorption energy of CO on Cu(100), Cu(111), Cu(211), and Cu(532), is calculated to be −1.08, −1.21, −1.13, and −1.18 eV, respectively. The adsorption of CO only slightly affects the barriers for the creation of Cu–adatoms on Cu(111) and Cu(100). The barrier for adatom formation is reduced by 0.20 eV on Cu(211) and 0.09 eV on Cu(532).

CO moderately affects the stability of the formed adatoms. The reaction energies for CO—Cu adatom formation on Cu(111) and Cu(100) are endothermic by 1.62 and 1.19 eV, whereas they are endothermic by 0.52 and 0.47 eV on Cu(211) and Cu(532), respectively. The adsorption of CO on the Cu adatoms lowers the diffusion barrier on the terraces for all surface orientations. We calculate the CO—Cu adatom forward diffusion barrier for Cu(100), Cu(111), Cu(211), and Cu(532), to be 0.45, 0.06, 0.22, and 0.40 eV, respectively.

To conclude, the adatoms are preferably formed on under-coordinated sites. The barriers for the adatom formation are generally decreased in the presence of CO. The adatom–CO complex is stabilized as compared to the adatom in the absence of CO. Hence, CO alters both the thermodynamics and the kinetics of the process. Importantly, the healing of the vacancy is preferred over the adatom diffusion away from the vacancy in the absence of CO, whereas the adatom–CO complex diffusion barrier away from the vacancy is similar to the barrier for CO-mediated healing of the vacancy. Adatoms are stabilized by clustering into larger islands on (111) and (100) facets. The PESes in Figure 2 are for the (211) and (532) facets constructed with cluster formation on (111). It is clear that instead forming a tetramer on (100) would result in a higher stabilization. A favorable pathway for cluster formation on NPs is, thus, vacancy formation on under-coordinated sites and clustering on the (100) facets.

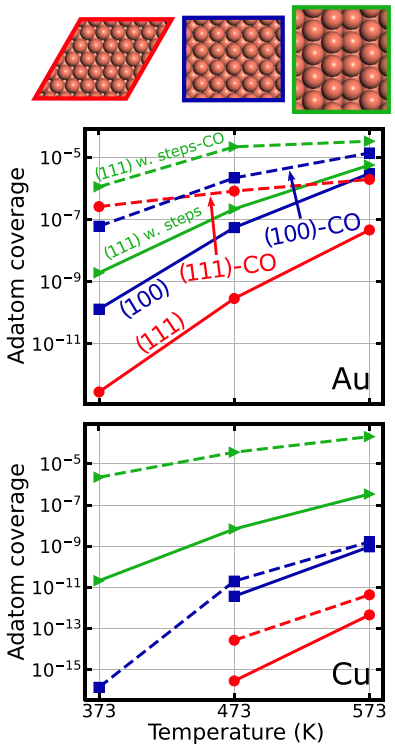


**FIGURE 3** | The adatom coverage on the (111) surface [red], the (100) surface [blue], and the (111) surface with two (211) steps [green], at 373, 473, and 573 K, for Au (top) and Cu (bottom). The coverages in the absence of CO are represented with continuous lines, whereas the dashed lines are the coverages at a CO pressure of 1 bar.

### 3.2 | Temperature-Dependent Adatom Coverage on Extended Surfaces

Kinetic Monte Carlo simulations are used to study adatom formation as a function of temperature. The considered surfaces are $p(20\times20)$ surfaces of (111) and (100), and a $p(20\times20)$ (111) surface with two (211) steps. All structures are created with 10 atomic layers, of which the bottom 8 layers are treated as bulk. The kMC simulations are performed in the absence of CO and with a CO pressure of 1 bar. The time-averaged coverage of adatoms at the temperatures 373, 473, and 573 K are presented for Au (top) and Cu (bottom) in Figure 3. The reaction conditions are, e.g., relevant for CO and $CO_2$ hydrogenation and additional results for 0.1 and 10 bar CO pressure are presented in Table S8. The results are averages of 16 independent simulations. The solid lines are the results for the (111) surface [red], the (100) surface [blue], and the (111) surface with two (211) steps [green] without CO. The average adatom coverages with CO are shown with dashed lines.

The coverage of adatoms on Au(111) in the absence of CO is below 1e-12 ML for $T$ = 373 K. The low coverage of adatoms (and vacancies) on the (111) surface is related to the high barrier for adatom formation, and the low stability of the adatom; a created adatom preferably heals the vacancy than diffuses away. The adatom coverage increases monotonically with temperature, however, the adatom coverage is low also at 573 K, being only ~ 5e-8 ML. The adatom formation process is more facile on Au(100) as compared to Au(111). However, also in this case, the healing of the vacancy is favored over the diffusion of the adatom away from the site where it was created. The rate of adatom diffusion away from the vacancy can be approximated as

$$r_{\text{diff.}} \propto \theta_{\text{adatom}}\, e^{-\Delta E^{\ddagger}_{\text{diff.}}/k_B T} \approx e^{-\Delta E_{\text{vac.form.}}/k_B T} e^{-\Delta E^{\ddagger}_{\text{diff.}}/k_B T}, \qquad (10)$$

where $\theta_{\text{adatom}}$ is the coverage of adatoms, $\Delta E^{\ddagger}_{\text{diff.}}$ is the barrier for adatom diffusion away from the vacancy and $\Delta E_{\text{vac.form.}}$ is the reaction energy for the vacancy formation. The ratio of adatom diffusion rates away from the vacancy ($r_{\text{diff.}}$) between Au(100) and Au(111) is ~ 100 at 373 K and about 20 at 573 K. This is consistent with the adatom coverages in Figure 3. When two (211) steps are introduced to the (111) surface, the adatom coverage is increased, owing to the facile vacancy formation process at the low-coordinated step sites. However, the healing of the vacancy is fast, and the adatoms are, consequently, short-lived. At 573 K, the adatom coverage is slightly below 1e-5 ML.

CO increases the presence of adatoms for all considered surfaces, with the largest effect for Au(111). The reason for the large effect on the Au(111) surface is the high coordination of the initial state. The coordination of Au in the (111) surface is nine, whereas the coordination of Au in the transition state of the vacancy formation is two. The low coordination of the transition state increases the adsorption strength of CO, which stabilizes the transition state. CO has a similar effect on the vacancy formation on Au(100) and at the (211) step. Furthermore, CO significantly stabilizes the adatom as compared to CO adsorbed on the metal atom in the surface. The metal–CO complex diffusion is facile, with rates similar to the healing of the vacancy. This is in contrast to the case without CO, where the vacancy healing process is faster. In similarity to the case without CO, the adatom coverage increases monotonically in the entire temperature range. At higher temperatures, the coverages are similar to the case without CO as CO desorbs at higher temperatures, preventing the CO-mediated processes to occur.

The adatom coverage at $T$ = 373 K is effectively zero for Cu(111) and Cu(100) in the absence of CO. This is consistent with the high barriers (1.8 eV) and endothermicity for adatom formation in these systems. At $T$ = 473 K, the calculated coverage for Cu(111) is about $10^{-16}$ ML, whereas the coverage of the Cu(100) is about $10^{-12}$ ML. The higher coverage on Cu(100) can be understood from the higher barrier for vacancy healing on Cu(100) [0.57 eV] as compared to Cu(111) [0.16 eV], Thus, the lifetime of adatoms is longer on Cu(100) than on Cu(111). As for the Au systems, the adatom coverage increases with temperature. The introduction of Cu(211) steps to the Cu(111) surface significantly affects the formation of adatoms. At $T$ = 373 K, the average coverage is around $10^{-11}$ ML and increases with temperature. The large difference in coverages between the Cu(111) and the stepped surface is related to differences in the barriers for adatom formation for the two surfaces. The ratio in the rates for adatom diffusion away from the vacancy (Equation 10) between a stepped Cu(111) surface and an extended Cu(111) surface is approximately $10^5$, which is close to the ratio of the coverages ($10^6$) obtained in the kMC simulations.

The introduction of a CO pressure increases the average adatom coverage for all surfaces, with the largest effect for the (111) surface with (211) steps. The coverage of adatoms increases in this case

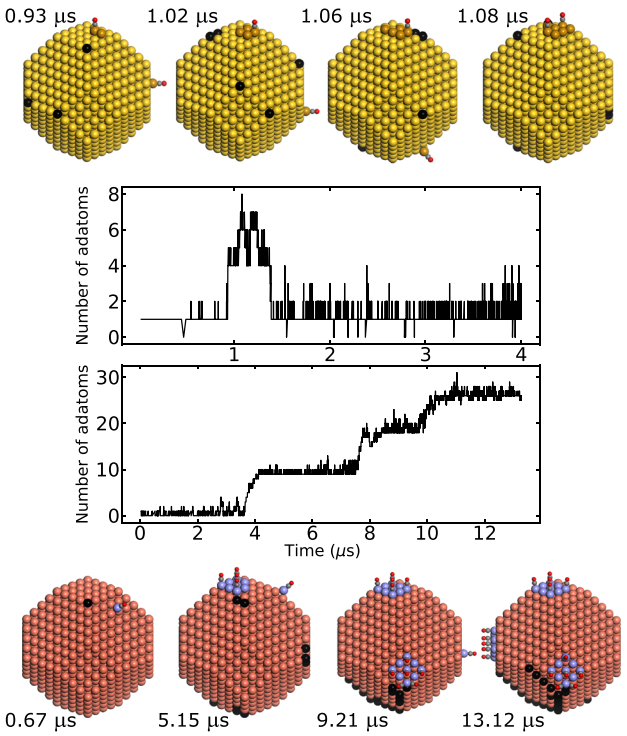


**FIGURE 4** | The number of adatoms as a function of time for Au (top) and Cu (bottom) truncated octahedron nanoparticles at 573 K and a CO pressure of 1 bar. Structures of the nanoparticles at different times are presented. In the snapshots, black color indicates a vacancy in the surface. For clarity, only CO adsorbed on adatoms are visualized.

by six, four and two orders of magnitude for 373, 473, and 573 K, respectively. The effect of CO on adatom formation is smaller for Cu(111) and Cu(100) as compared to the corresponding surfaces for Au. This is a consequence of the lower stabilization of the vacancy formation energy by CO on Cu as compared to Au and by the overall higher barriers for the adatom formation process on Cu. The result that CO facilitates adatom formation is agreement with a recent report on the CO-induced roughening of Cu(111) [35].

### 3.3 | Adatom Cluster Formation on NPs

Kinetic Monte Carlo simulations are performed for a 3.6 nm truncated octahedron Au and Cu nanoparticle with a CO pressure of 1 bar at 573 K. The truncated octahedron is the stable Wulff-construction of NPs of this size for both Au and Cu. In Figure 4, the number of adatoms (and vacancies) are presented as a function of time for Au (top) and Cu (bottom). Snapshots of the nanoparticles at four different instances are included, in which black color indicates a vacancy. Adsorbed CO is visualized only on the adatoms for clarity.

When a vacancy is formed on the surface, the neighboring surface atoms get a lower coordination, which decreases the barrier for the formation of a second adatom. Moreover, neighboring adatoms on the facets of the NP stabilize adatoms by the formation of clusters and thereby alter the thermodynamic preference for adatom formation. For the Au NP, three adatoms have formed at 0.93 $\mu$s. Two adatoms have clustered, forming a dimer on the Au(100) facet, whereas the third adatom diffuses in the form of an Au—CO complex. The vacancies are located in the corner of the nanoparticle as a result of the lower coordination and stability of these atoms. At 1.03 $\mu$s, four adatoms have clustered on an Au(100) facet, forming a tetramer. The tetramer has an enhanced stability, as all adatoms in the cluster are six-fold coordinated. Note that also two of the vacancies have clustered, as this also lowers the energy. The adatom cluster grows to as many as eight adatoms until it eventually disintegrates. The monomeric adatoms are always covered with CO, and the Au—CO complex diffusion is facile. However, CO desorbs from the larger clusters owing to the higher coordination of the adatoms and the repulsive CO—CO interactions. The time-scale of the cluster formation and disintegration is on the order of microseconds, which could make these transient structures difficult to observe experimentally.

The clusters formed on the Cu NP in Figure 4 are large and stable. Once a nine-atom cluster has formed, it remains until the end of the simulation. The first cluster in the trajectory is formed after 4 $\mu$s. In similarity with Au, a tetramer on (100) is the required unit to form larger islands. As for Au, CO desorbs from the adatoms once the clusters form on the surface. CO is on the nine-atom clusters occupying only the corner sites. It should be noted that not all trajectories result in three 9-atom islands that are stable over the entire simulation time. We have also obtained trajectories with zero, one and two islands.

The possibility to form Cu islands on the (100) is related to the higher stability of the islands on the (100) facets as compared to the (111) facets (coordination number four instead of three) combined with the higher barrier for adatom diffusion on (100) as compared to (111). The slow diffusion on (100) increases the lifetime of the clusters. Even though the corner sites on the nine-atom cluster are as undercoordinated as the regular corner on the nanoparticle, these atoms are stabilized by the overall energy gain from CO adsorption. Adatoms originate predominantly from corner sites. The loss of coordination for neighboring atoms, once a vacancy has formed, leads to an etching of the edges of the NP. The accumulation of vacancies on the edges of the nanoparticle is visible at the snapshots at 9.21 $\mu$s and 13.12 $\mu$s.

The reason for the transient clusters on the Au NP is a consequence of the stable initial structure. Even if CO alters the kinetics and the stability of adatoms, it does not alter the preferred structure as CO adsorption is endergonic (positive Gibbs free energy of adsorption) for all sites with CN > 6, and only slightly exergonic for sites with CN < 6 at 573 K. Thus, there is no thermodynamic driving force for NP reconstruction at this temperature. In contrast, CO adsorption on Cu NPs may alter the thermodynamically preferred structure. In the absence of CO, relocating nine Cu atoms from the corners of the truncated octahedron to form a cluster on the (100) facet is endergonic. However, the relocation of atoms from the corners creates new under-coordinated sites with strong CO adsorption energies. The free energy gain for the process can be approximated as follows:

$$\Delta G = \sum_i \Delta N_i \, \theta_i \, \Delta G_i, \tag{11}$$

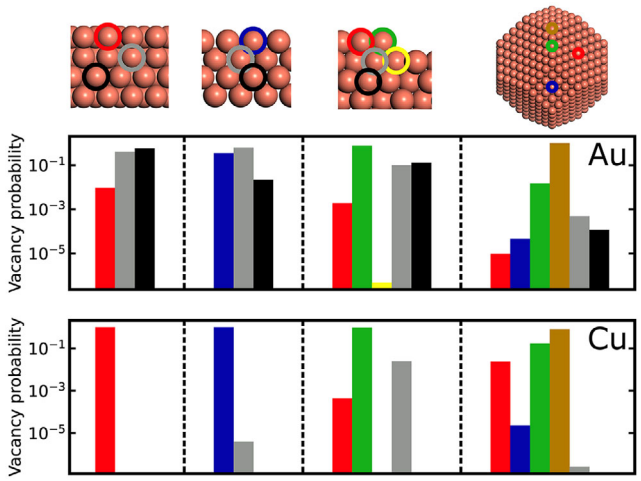


**FIGURE 5** | The distribution of vacancies for the (111) surface, the (100) surface, the (111) surface with two (211) steps and a 3.6 nm truncated octahedron nanoparticle at 473 K and a CO pressure of 1 bar for Au (top) and Cu (bottom). Vacancy color codes: Red [surface site of (111) facet], blue [surface site of (100) facet], green [step or edge site], brown [corner site], gray [second layer], yellow [10-fold atom in (211)] and black [third layer or bulk]. The results are averages of 16 independent kMC simulations.

where the summation runs over all coordination numbers for which the CO adsorption is exergonic, $\Delta N_i$ is the change in the number of atoms with CN corresponding to $i$, $\theta$ is the corresponding CO coverage (which can be estimated with a Langmuir isotherm), and $\Delta G$ is the Gibbs free energy of adsorption. In the case of nine corner atoms clustering on a (100) facet, the thermodynamic driving force, originating from the increased CO adsorptions, is approximately −2.2 eV for the Cu NP, which compensates the endergonity in the loss of metal–metal interactions, which is 1.8 eV. Thus, CO alters both the kinetics and the thermodynamics of the NP reconstruction for Cu, leading to a difference in the structural stability with and without a CO pressure.

### 3.4 | The Distribution of Vacancies

The creation of adatoms on the surface is associated with the simultaneous creation of vacancies. Once an adatom is formed, it can either diffuse away or heal the vacancy. The vacancy can, in addition, be healed by lateral atom diffusion within the surface plane or by diffusion of subsurface atoms. Knowledge about the distribution of the vacancies is crucial for several reasons. Vacancies at different locations in the surface alters the coordination and, hence, the chemical properties of neighboring atoms. The location of the vacancies may also influence the adatom coverage, as vacancies in the surface layer are more readily healed than subsurface and bulk vacancies.

The time-averaged vacancy occupations for the different types of sites for all considered systems are shown in Figure 5. For M(100) and M(111), the vacancy can occupy three non-equivalent types of surface sites, namely (i) surface, (ii) subsurface, and (iii) bulk (layer 3 and deeper). The surface with a step has, in addition, two nonequivalent sites: (i) a surface edge and (ii) a 10-fold surface site. The NP system has, in addition to the sites on the M(111) and M(100) surfaces, two additional sites in the topmost layer: the edge and the corner sites.

The results in Figure 5 are averages of 16 independent simulations performed at 473 K and a CO pressure of 1 bar. Red and blue colors indicate a vacancy in a (111) facet and a (100) facet, respectively. The green color represents a vacancy on a step or at an edge of a nanoparticle. The brown color is a vacancy on the corner of the nanoparticle. Note that close to a (211) step, 10-fold coordinated atoms are present, and the vacancy in those positions is represented with the yellow color. Gray color indicates a subsurface vacancy (second layer), whereas black indicates a vacancy in the third layer or the bulk.

For the extended Au(111) and Au(100) surfaces, the vacancies are preferably located subsurface, and the vacancies are rarely located in the surface layer. The preference for subsurface vacancies has a thermodynamic origin. Diffusion of Au from the surface layer in Au(111) to the second layer is associated with a barrier of 0.40 eV, whereas the diffusion from the second layer to a vacant site in the surface is associated with a barrier of only 0.24 eV. The vacancy is, hence, more stable in subsurface positions. The preference for subsurface vacancies is consistent with the tendency of Au clusters to form hollow structures [36] and the pronounced *d*-character in the Au—Au bond [37].

The adatom coverage and number of vacancies are increased when the (211) steps are introduced to the (111) surface. The vacancies are in this case preferably located on the (211) step, as a result of the lower coordination. However, a large fraction of vacancies are still present below the (111) terraces. The same preference is present for the NP. Vacancies are preferably located at the corners of the particle, where the atom stability is the lowest. However, also edge vacancies are present. Subsurface vacancies are rare for the NP, although they are present below the (111) and (100) terraces.

The distribution of vacancies for Cu(111) and Cu(100) is different than for the corresponding Au systems. For the extended Cu(111) and Cu(100) surfaces, the vacancies are located mostly in the surface layer. In fact, all vacancies are found on the topmost layer for Cu(111), whereas some vacancies are present also in the subsurface layer for Cu(100). The preference of vacancies in the surface layer has thermodynamic origin. The barrier for Cu diffusion from the surface layer to the subsurface is 0.35 and 0.16 eV for Cu(111) and Cu(100), respectively. The barrier for Cu diffusion from the subsurface layer to the surface is 0.70 and 0.68 eV for Cu(111) and Cu(100), respectively.

The introduction of the two (211) steps on the Cu(111) surface slightly modifies the vacancy distribution. As for the Au system, vacancies are generally located at the steps. Note that the number of vacancies (and adatoms) is significantly larger for the stepped Cu(111) surface than on (111) surfaces (Figure 3). Interestingly, the presence of the steps also increases the probability of subsurface vacancies in the second layer. The vacancy distribution for the Cu NP is similar to that of Au in the sense that the vacancies are generally located at the corner and step sites. However, the presence of subsurface vacancies in the Cu NP is low.

## 4 | Conclusions

Technical catalysts are commonly realized as 2–5 nm-sized metal NPs supported on porous supports. NPs in this size regime are structurally flexible and respond sensitively to the operating conditions. In this work, we have used a 3D DFT-based kinetic Monte Carlo approach to investigate the flexibility of Au and Cu NPs in a CO atmosphere. CO is found to promote the presence of adatoms and the formation of small two-dimensional clusters. The work highlights the interplay between kinetics and thermodynamics for the flexibility of the NPs. The kinetics determines how facile the reactions are, whereas the thermodynamics determines the stability. The simulations show that catalyst particles adapt their structure to the reaction conditions and that new catalyst sites are created during the reaction. The restructuring could have implications for catalytic reactions, as reaction barriers on metal systems depend on the coordination numbers.


### Acknowledgments

Financial support is acknowledged from the Swedish Research Council (2024-05250) and The Wallenberg Initiative Material Science for Sustainability (WISE). The calculations were performed at NSC via a NAISS grant (NAISS 2024/3-26). The Competence Centre for Catalysis (KCK) is hosted by Chalmers University of Technology and is financially supported by the Swedish Energy Agency and the member companies Johnson Matthey, Perstorp, Powercell, Preem, Scania CV, Umicore, and Volvo Group.


### Conflicts of Interest

The authors declare no conflict of interest.

### References


1. P. L. Hansen, J. B. Wagner, S. Helveg, J. R. Rostrup-Nielsen, B. S. Clausen, and H. Topsøe, "Atom-Resolved Imaging of Dynamic Shape Changes in Supported Copper Nanocrystals," *Science* 295, no. 5562 (2002): 2053–2055.

2. A. Ricchebuono, E. Vottero, D. Bonavia, et al., "Co-Induced Dynamic Behavior of $Al_2O_3$-Supported Pd Nanoparticles at Room Temperature," *ACS Catalysis* 14 (2024): 13736–13746.

3. F. Mittendorfer, N. Seriani, O. Dubay, and G. Kresse, "Morphology of Mesoscopic Rh and Pd Nanoparticles Under Oxidizing Conditions," *Physical Review B* 76 (2007): 233413.

4. Y. Suchorski, J. Zeininger, S. Buhr, et al., "Resolving Multifrequential Oscillations and Nanoscale Interfacet Communication in Single-Particle Catalysis," *Science* 372, no. 6548 (2021): SI, 1314–1318.

5. X. Zhou, W. Xu, G. Liu, D. Panda, and P. Chen, "Size-Dependent Catalytic Activity and Dynamics of Gold Nanoparticles at the Single-Molecule Level," *Journal of the American Chemical Society* 132, no. 1 (2010): 138–146.

6. H. Eliasson, Y. Niu, R. E. Palmer, H. Grönbeck, and R. Erni, "Support-Facet-Dependent Morphology of Small Pt Particles on Ceria," *Nanoscale* 15 (2023): 19091–19098.

7. Y.-G. Wang, D. Mei, V.-A. Glezakou, J. Li, and R. Rousseau, "Dynamic Formation of Single-Atom Catalytic Active Sites on Ceria-Supported Gold Nanoparticles," *Nature Communications* 6 (2015): 6511.

8. C. J. Owen, N. Marcella, C. R. O'Connor, et al., "Surface Roughening in Nanoparticle Catalysts," (2024). [Online]. Available, https://arxiv.org/abs/2407.13643.

9. S. Yang, S. Li, W. Zhang, L. Luo, and X. Chen, "Insights Into the Dynamics of Supported Au Nanoparticles in the Wet Environments From First-Principles and ReaxFF MD Simulations," *Applied Surface Science* 679 (2025): 161232.

10. J. R. Boes and J. R. Kitchin, "Modeling Segregation on AuPd(111) Surfaces With Density Functional Theory and Monte Carlo Simulations," *Journal of Physical Chemistry C* 121 (2017): 3479–3487.

11. L. Li, X. Li, Z. Duan, et al., "Adaptive Kinetic Monte Carlo Simulations of Surface Segregation in PdAu Nanoparticles," *Nanoscale* 11 (2019): 10524–10535.

12. Z. Zhang, W. Gee, P. Sautet, and A. N. Alexandrova, "H and Co Co-Induced Roughening of Cu Surface in $CO_2$ Electroreduction Conditions," *Journal of the American Chemical Society* 146, no. 23 (2024): 16119–16127. [Online]. Available, https://doi.org/10.1021/jacs.4c03515.

13. C. Waldt, R. Kumar, and D. Hibbitts, "Understanding AuPd Alloy Nanoparticle Structure Under Vacuum Using DFT and Monte Carlo Methods," *Journal of Physical Chemistry C* 129 (2025): 5702–5717.

14. E. Sireci, T. D. Grüger, P. N. Plessow, D. I. Sharapa, and F. Studt, "Modeling the Shape and Stability of CO Nanoparticles as a Function of Size and Support Interactions Through DFT Calculations and Monte Carlo Simulations," *Journal of Physical Chemistry C* 129, no. 29 (2025): 13232–13243.

15. A. Bruix, J. T. Margraf, M. Andersen, and K. Reuter, "First-Principles-Based Multiscale Modelling of Heterogeneous Catalysis," *Nature Catalysis* 2 (2019): 659–670.

16. M. Jørgensen and H. Grönbeck, "Perspectives on computational catalysis for metal nanoparticles," *ACS Catalysis* 9 (2019): 8872–8881.

17. B. W. J. Chen, L. Xu, and M. Mavrikakis, "Computational methods in heterogeneous catalysis," *Chemical Reviews* 121 (2021): 1007–1048.

18. L. Xu, K. G. Papanikolaou, B. A. J. Lechner, et al., "Formation of Active Sites on Transition Metals Through Reaction-Driven Migration of Surface Atoms," *Science* 380, no. 6640 (2023): 70–76.

19. R. Svensson and H. Gronbeck, "Dynamics of Dilute Nanoalloy Catalysts," *Journal of Physical Chemistry Letters* 15, no. 31 (2024): 7885–7891.

20. X.-Y. Li, P. Ou, X. Duan, et al., "Dynamic Active Sites In Situ Formed in Metal Nanoparticle Reshaping Under Reaction Conditions," *Journal of the American Chemical Society Au* 4 (2024): 1892–1900.

21. G. Kresse and J. Hafner, "Ab Initio Molecular Dynamics for Liquid Metals," *Physical Review B* 47, no. 1 (1993): 558.

22. G. Kresse and J. Hafner, "Ab Initio Molecular Dynamics for Open-Shell Transition Metals," *Physical Review B* 48, no. 17 (1993): 13115.

23. G. Kresse, "Ab Initio Molecular-Dynamics Simulation of the Liquid-Metal–Amorphous-Semiconductor Transition in Germanium," *Physical Review B* 49, no. 20 (1994): 14251.

24. G. Kresse and J. Furthmüller, "Efficient Iterative Schemes for Ab Initio Total-Energy Calculations Using a Plane-Wave Basis Set," *Physical Review B* 54, no. 16 (1996): 11169.

25. P. E. Blöchl, "Projector Augmented-Wave Method," *Physical Review B* 50, no. 24 (1994): 17953.

26. G. Kresse and D. Joubert, "From Ultrasoft Pseudopotentials to the Projector Augmented-Wave Method," *Physical Review B* 59, no. 3 (1999): 1758.

27. J. P. Perdew, K. Burke, and M. Ernzerhof, "Generalized Gradient Approximation Made Simple," *Physical Review Letters* 77, no. 18 (1996): 3865.

28. S. Grimme, J. Antony, S. Ehrlich, and H. Krieg, "A Consistent and Accurate Ab Initio Parametrization of Density Functional Dispersion Correction (DFT-D) for the 94 Elements H-Pu," *Journal of Chemical Physics* 132, no. 15 (2010): 154104.

29. S. Grimme, S. Ehrlich, and L. Goerigk, "Effect of the damping function in dispersion corrected density functional theory," *Journal of Computational Chemistry* 32, no. 7 (2011): 1456–1465.

30. G. Henkelman and H. Jónsson, "Improved Tangent Estimate in the Nudged Elastic Band Method for Finding Minimum Energy Paths and

Saddle Points," *Journal of Chemical Physics* 113, no. 22 (2000): 9978–9985.

31. G. Henkelman, B. P. Uberuaga, and H. Jónsson, "A Climbing Image Nudged Elastic Band Method for Finding Saddle Points and Minimum Energy Paths," *Journal of Chemical Physics* 113, no. 22 (2000): 9901–9904.

32. A. P. J. Jansen, *An Introduction to Kinetic Monte Carlo Simulations of Surface Reactions* vol. 856 (Springer, 2012).

33. M. Jørgensen and H. Grönbeck, "Montecoffee: A Programmable Kinetic Monte Carlo Framework," *Journal of Chemical Physics* 149, no. 11 (2018): 114101.

34. I. Chorkendorff and J. W. Niemantsverdriet, *Concepts of Modern Catalysis and Kinetics* (John Wiley & Sons, 2017).

35. K. G. Papanikolaou, L. Xu, E. Smith, and M. Mavrikakis, "Co-Induced Roughening of Cu(111): Formation and Detection of Reactive Nanoclusters on Metal Surfaces," *Surface Science* 754 (2025): 122665.

36. X. Xing, B. Yoon, U. Landman, and J. H. Parks, "Structural Evolution of Au Nanoclusters: From Planar to Cage to Tubular Motifs," *Physical Review B* 74, no. 16 (2006): 165423.

37. H. Grönbeck and P. Broqvist, "Comparison of the Bonding in $Au_8$ and $Cu_8$: A Density Functional Theory Study," *Physical Review B* 71 (2005): 073408.

## Supporting Information

Additional supporting information can be found online in the Supporting Information section.

**Supporting File**: cctc70535-sup-0001-SuppMat.pdf.